Efficient Ribcage Segmentation from CT Scans Using Shape Features

Ziyue Xu, Ulas Bagci*, Colleen Jonsson, Sanjay Jain, and Daniel J. Mollura

***Abstract*— Rib cage structure and morphology is important for anatomical analysis of chest CT scans. A fundamental challenge in rib cage extraction is varying intensity levels and connection with adjacent bone structures including shoulder blade and sternum. In this study, we present a fully automated 3-D algorithm to segment the rib cage by detection and separation of other bone structures. The proposed approach consists of four steps. First, all high-intensity bone structures are segmented. Second, multi-scale Hessian analysis is performed to capture plateness and vesselness information. Third, with the plate/vessel features, bone structures other than rib cage are detected. Last, the detected bones are separated from rib cage with iterative relative fuzzy connectedness method. The algorithm was evaluated using 400 human CT scans and 100 small animal images with various resolution. The results suggested that the percent accuracy of rib cage extraction is over 95% with the proposed algorithm.**

***Index Terms*— Rib cage segmentation, multi-scale Hessian analysis, iterative relative fuzzy connectedness**

I. Introduction

Accurate and robust segmentation of the rib cage from CT images is of significant clinical value. The structure and morphology of rib bones can serve as a stable reference for multiple analysis and quantification tasks including lung volume estimation, organ localization, and bone abnormality quantification. As 3-D tubular structures, manual identification of rib cage is a tedious and time consuming task. Therefore, automatic segmentation algorithms are necessary for reliable localization and assessment of rib bones. Many algorithms have been proposed for rib cage segmentation in the literature. Most of them make use of existing general elongated structure segmentation techniques that can also be applied for vasculature scenario. For instance, in [1], a 3-D region growing algorithm is proposed with local adaptive thresholding for skeletal structure segmentation. In [2], seed points for ribs are first identified in from central slice, and centerline tracing algorithm is subsequently utilized for extracting individual ribs. A classification based method was further presented in [3], where a classifier was trained to distinguish the primitives in ribs and background. Recently, centerline of the spinal canal is employed to generate seed region for every rib in [4], and region growing is further performed to extract rib structures. Another tracking method was reported in [5] where anatomical and other prior knowledge were added to assist the process.

*This research is supported by CIDI, the intramural research program of the National Institute of Allergy and Infectious Diseases (NIAID) and the National Institute of Biomedical Imaging and Bioengineering (NIBIB).

Z. Xu, U. Bagci, and D. J. Mollura are with Center for Infectious Disease Imaging, Radiology and Imaging Sciences, National Institutes of Health, Bethesda, MD; C. Jonsson is with University of Louisville, Louisville, KY; S. Jain is with Johns Hopkins University, Baltimore, MD.

Almost all previous methods follow the "adding" model, i.e., increasingly capturing the voxels that belong to rib structure. While such approach works well for many cases, it may be limited by two major challenges of growing-based methods: early termination (false negative) and leakage (false positive). Large variations in the appearance, resolution, and pathology of bones also contribute to limited robustness for model-based methods. Therefore, in this paper, instead of "adding", we focus on a "subtracting" model. All bone structures are first segmented, then extra bones such as shoulder blade and sternum are detected and discarded from the previous segmentation, resulting in rib cage alone. Our method makes use of the priori shape information from different bone structures within chest CT scans, and is fully automatic and model-free.

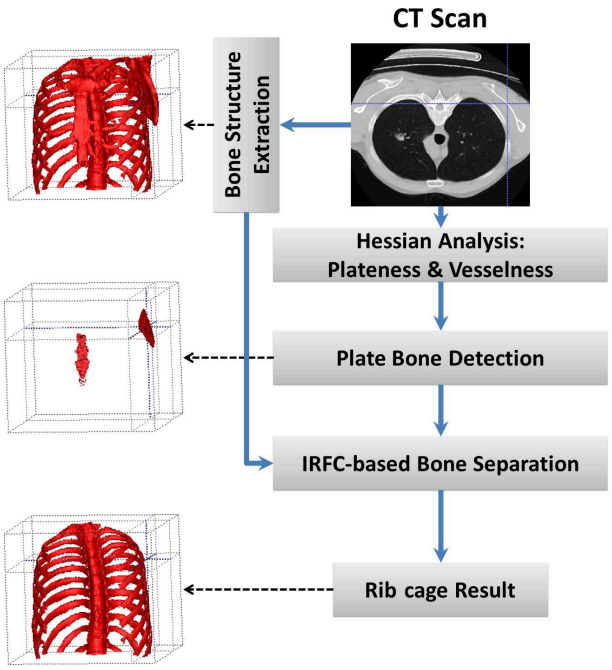

Fig. 1. Flowchart of the rib cage segmentation algorithm

Fig. 1 illustrates the flowchart of the proposed method. As can be noticed, the proposed method segments the rib cage by removing the "irrelevant" bone structures from the whole bone extraction. First, all connected bone structures are detected using fuzzy connectedness (FC) method, including rib cage, sternum, clavicle, and scapula. Then, plateness and vesselness are calculated via Hessian analysis to enhance the plate-like bones of sternum and scapula while excluding tubular ribs. Next, plate-like bones are detected based on the plateness and vesselness information. Last, rib cage

is separated from whole bone segmentation with iterative relative fuzzy connectedness (IRFC) method, resulting in the final rib cage segmentation.

II. Theory and Algorithms

In this section, we first briefly present the theory of FC [6] and IRFC [7]. Then, details of vesselness and plateness computation based on Hessian analysis [8] is provided. Subsequently, the theory and algorithm of the proposed method is formulated that combines the above methods to capture rib cage.

A. FC Segmentation

Under FC framework, a fuzzy topological description at every image location characterizes how the voxels hang together locally with their neighbors to form an object. This notion is defiend through a predefined function called *affinity* ([6]). Let $\mathcal{V} \subset \mathbb{Z}^3$ denotes a 3-D cubic grid representing the *image space*, where each element of $\mathcal{V}$ is a *voxel*, an *adjacency* relation (μ_α) can be defined such that it determines which pairs of voxels are close enough to be considered connected: $\mu_\alpha : \mathcal{V} \times \mathcal{V} \rightarrow \{0, 1\}$. Theoretically, if p and q are α-adjacent to each other, then $\mu_\alpha(p, q) = 1$, '0' otherwise. In practice, we set $\alpha = 26$ for adjacency in 3-D analysis. While affinity is intended to be a local relation, a global fuzzy relation called fuzzy connectedness is induced on the image domain by the affinity functions. This is done by considering all possible paths between any two voxels p and q in the image, and assigning the strength of fuzzy connectedness according to the strongest path between p and q.

The *affinity* κ is the most fundamental measure of local hanging togetherness of nearby voxels. For a path π, which is a sequence of voxels $\langle p_1, p_2, ..., p_l \rangle$ with every two successive voxels being adjacent, given *fuzzy affinity function* $\mu_\kappa(p_i, p_{i+1})$, the strength of the path is defined as the minimum affinity along the path:

$$\mu_\mathcal{N}(\pi) = \min_{1 \leq i < l} \mu_\kappa(p_i, p_{i+1}). \tag{1}$$

Then, the strength of connectedness $\mu_\mathcal{K}(p, q)$ between any two voxels p and q is the strength of the strongest path between them as

$$\mu_\mathcal{K}(p, q) = \max_{\pi \in \mathcal{P}(p,q)} \mu_\mathcal{N}(\pi), \tag{2}$$

where $\mathcal{P}(p, q)$ denotes the set of all paths between p and q. Therefore, a fuzzy connected object $\mathcal{O}$ in an image can be defined for a predetermined set of seeds S. Since the level of FC between any two voxels p and q is considered to be the maximum of the strengths of all paths between them, for multiple seeds, the fuzzy object membership function for $\mathcal{O}$ or the strength of connectedness of $\mathcal{O}$ is defined as follows:

$$\mu_\mathcal{O}(p) = \max_{s \in S} \mu_\mathcal{K}(p, s). \tag{3}$$

An efficient computational solution is presented ([6]) for computing $\mu_\mathcal{O}(p)$, given κ and S and an image.

Absolute FC segmentation is based on computing the FC strength between a set of seed points and all other voxels within the image and set a proper threshold to the resulting FC image. For object and background with moderate contrast, it has been proven to be effective in segmentation. Hence, FC is employed to segment whole bone structures from CT images. The seed points are automatically initialized at voxels with Hounsfield unit (HU) intensity $> 800HU$. To avoid arbitrary threshold, relative fuzzy connectedness provides a solution where sets of seeds $S_n | n = 1, 2, ..., N$ are available for N different objects. Seeds compete among each other, and an voxel p is assigned to the object with the largest fuzzy connectedness strength as

$$L(p) = L(S_n), \ n = \arg\max_n \mu_{\mathcal{O}_n}(p), \tag{4}$$

where $L(p)$ provides the label of voxel p. Relative FC can be regard as the extension of FC when multiple seeds are available for different objects. The basic computation remains the same, the label of voxels can be automatically assigned.

One challenge for FC is that the performance can be limited for cases where different objects have similar intensity and separated by low contrast gaps. For this study, plate bones need to be separated from ribs at their connection locations, and the interval between them is often narrow with low contrast. Therefore, the sensitivity and specificity of absolute FC or relative FC can be limited. Here, we further use iterative relative FC that leads to more effective segmentations using relative FC with two seed sets of plate-like bones and rib cage. The basic idea is to iteratively identify the range of each object through relative connectedness, and the identified range is then excluded from being considered by other objects for path tracking. Hence, this method keeps track of the growing process from each seed sets and effectively minimizes the strong paths going through the object of interest, so that structures with similar intensities can be separated. See [7] for more details.

B. Multi-Scale Hessian Analysis

In 3-D CT images, ribs can be regarded as bright tubular structures on the dark background, while sternum and scapula can be described as bright plate-like structures. Identification and delineation of such structures can be improved by enhancement algorithms. As shown in [8], analyzing the second-order information (Hessian) of a Gaussian convoluted image provides local information of the structure. Specifically, eigenvalue decomposition is performed over the Hessian matrix and the resulting ordered eigenvalues, i.e., $(|\lambda_1| \leq |\lambda_2| \leq |\lambda_3|)$, are examined. For tubular structures, it was expected that λ_1 was small and the other two were large and of equal sign; while for plate structures, it was expected that both λ_1 and λ_2 were small and λ_3 was large. Explicitly, for a bright structure on a dark background, *vesselness* can be formulated as

$$V_\sigma = \begin{cases} 0, & \text{if } \lambda_2 > 0 \text{ or } \lambda_3 > 0; \\ (1 - e^{-\frac{R_A^2}{2\alpha^2}}) e^{-\frac{R_B^2}{2\beta^2}} (1 - e^{-\frac{S^2}{2\gamma^2}}), & \text{else,} \end{cases} \tag{5}$$

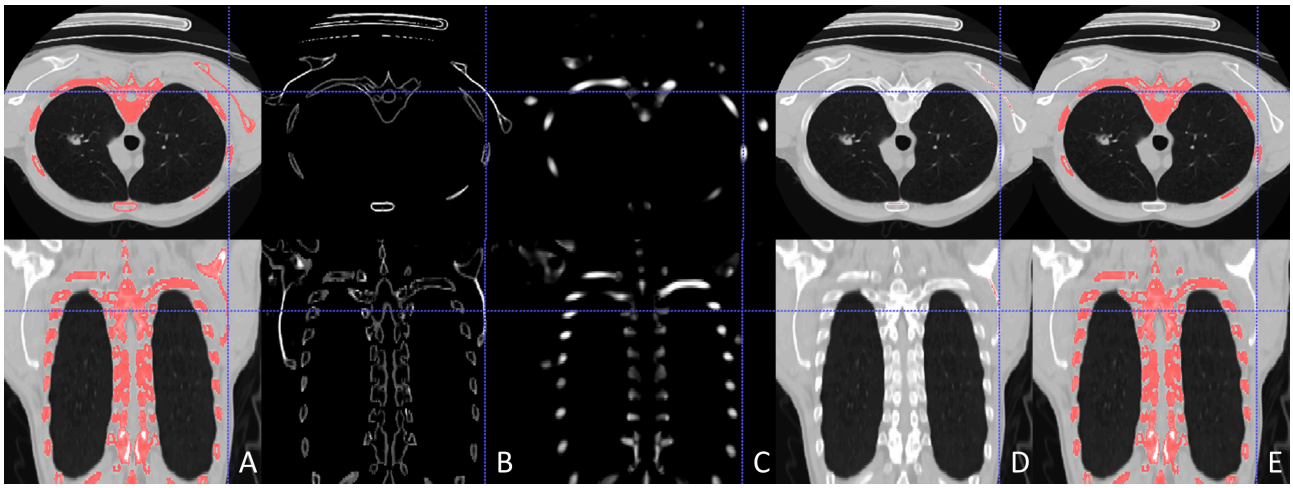

Fig. 2. Example axial (first row) and coronal (second row) slices for each step of the proposed method. (A) Original CT image with whole bone segmentation (the largest connected group is selected). (B) Plateness computation result. (C) Vesselness computation result. (D) Detected plate-like structures. (E) Rib cage segmentation after separation.

where $R_A = |\lambda_2|/|\lambda_3|$, $R_B = |\lambda_1|/\sqrt{|\lambda_2\lambda_3|}$ and $S = \sqrt{\lambda_1^2+\lambda_2^2+\lambda_3^2}$; and *plateness* can be formulated as

$$P_\sigma = \begin{cases} 0, & \text{if } \lambda_3 > 0; \\ e^{-\frac{R_B^2}{2\beta^2}}(1-e^{-\frac{S^2}{2\gamma^2}}), & \text{else,} \end{cases} \tag{6}$$

where α, β, γ are parameters determined by user according to image and structural details, $R_B = |\lambda_2|/|\lambda_3|$, and $S = \sqrt{\lambda_1^2+\lambda_2^2+\lambda_3^2}$.

The vesselness and plateness measurements (i.e., V and P) were calculated at different scales (σ) and the maximum response was achieved at a scale that matches the size of the structure. Therefore, by using a multi-scale approach which covers a range of structure widths and finding the maximum value $V = \max(V_\sigma)$, $P = \max(P_\sigma)$, $\sigma_{\min} \le \sigma \le \sigma_{\max}$, we enhanced the local tubular and plate structures. For rib cage application, we first briefly estimated the minimum and maximum rib size according to normal rib radius and image spacing, and then set $\sigma_{\min}$ and $\sigma_{\max}$ accordingly.

C. Rib cage extraction

Let S denote the plate-like bones to be excluded and $\bar{S}$ denote the rib cage bones such that $B = S \cup \bar{S}$. S can be characterized by high P and low V responses, while $\bar{S}$ features high V and moderate P values. Therefore, thresholding was applied to extract candidate plate voxels $Sd_S \in S$ and rib voxels $Sd_{\bar{S}} \in \bar{S}$. Since Sd_S and $Sd_{\bar{S}}$ usually cover only part of the entire rib and scapula, these points were used as seed points to initiate a IRFC within the initial bone segmentation B. With IRFC, the two objects are separated at the low-intensity connection location, hence all voxels belonging to plate bones were excluded from rib cage segmentation.

As illustrated in Fig. 2, initial bone segmentation can contain scapula that is locally connected to rib cage (A). With plateness (B) and vesselness (C) enhancement, it is obvious that scapula can be detected and distinguished from rib structures using high plateness and low vesselness (D). Last, IRFC is employed to separate scapula from rib cage using seed point from (D), resulting in final rib cage segmentation (E). In this way, the region grow process for rib extraction, which can be limited by false negatives and false positives, is avoided. Also, seed points are assigned robustly within the candidate structures, ensuring efficient and accurate rib cage segmentation.

III. Results

To evaluate the performance of our rib cage segmentation method, we used 400 human and 100 small animal data sets. Images were acquired using 64-detector row Phillips Brilliance 64 or GE Medical Systems Light Speed Ultra. Scans were performed at end-inspiration with 1.0 or 2.0 collimation and obtained at 10 or 20 mm intervals from the base of the neck to upper abdomen. For human image, slice thickness ranges from 1 mm to 5 mm (200 of them have thickness 5 mm, 90 of them have thickness 2.5 mm and the rest have thickness < 2 mm), while in-plane resolution ranges from 0.5×0.5 mm to 0.8×0.8 mm. For small animal images (rabbits and ferrets), the spatial resolution range from 0.2×0.2 mm to 0.3×0.3 mm in plane and 0.2 mm to 0.6 mm between slices ([9], [10]).

For segmentation algorithm evaluation, manual delineation is often used as reference standard. However, for rib cage segmentation, as it appears tubular structures in 3-D space, it is tedious and time consuming for human to define the exact boundaries by tracing the voxels for the entire 3-D image. Here, we first performed a visual qualitative evaluation of all images by two experts for the performance of the proposed algorithm. Experts were asked to evaluate if rib cage has been extracted successfully by identifying errors including residual scapula (false positive) and mistakenly removed rib (false negative). The count of error-free cases is counted and comprised with the total image number as the success rate. Fig. 3 shows an example of the rib cage extraction

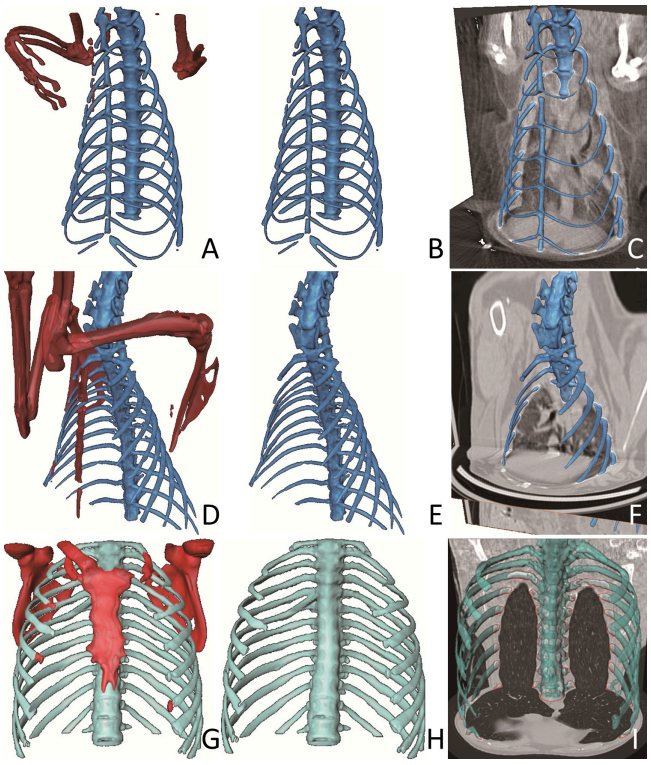

Fig. 3. 3-D Segmentation results on small animals (A-F) and human subject (G-I). (A, D, G) whole bone structure extraction result; (B, E, H) rib cage result after subtraction; (C, F, I) fused illustration of segmentation and CT image.

performance on small animals (rib shown in blue with other bone structure shown in red) (A-F) and human subject (rib shown in green with other bone structure shown in red) (G-I). (A, D, G) illustrates whole bone structure extraction result; (B, E, H) shows rib cage result after subtraction; and (C, F, I) are fused illustrations of segmentation and CT image. This example confirms the observation that the proposed method can successfully capture and exclude other bone structures from rib cage. The overall success rate is 95%, and no failure has been identified for small animal images given that there is better contast and larger separation. For the 27 unsuccessful cases, 24 of them have 5 mm thickness, one 2.5 mm and two below 2 mm. 16 of them suffers from major false positives, and 11 have mistakenly removed rib structure. Also, it appears that most of the unsuccessful cases are of low resolution and high noise/artifacts, which jeopardize the performance of IRFC due to local intensity variance and broken connectivity. As one future work to address this problem, extra step of manual intervention can be helpful in adding more accurate seed points, defining separation, and fine parameter tuning.

For quantitative evaluation, instead of manually tracing the rib structures, we selected 50 slices (45 human images and 5 small animal images) containing connection areas of rib cage and other bones, covering object, resolution, and appearance variations. Experts are asked to manually draw the separation curves between the rib cage and other bones on the overlapping whole bone segmentation. For quantification purpose, Hausdorff distance (HD) is computed between the result from proposed method and the reference. The experimental results showed that by applying the proposed IRFC method, the separation line can be accurately estimated, and the average HD is 0.7 pixels. The computation time including Hessian analysis and FC/IRFC computation is five minutes for an image with size $512\times512\times422$ on a 3.7 GHz machine running Linux system.

IV. Conclusion

A fully automated 3-D algorithm to segment the rib cage by detection and separation of other bone structures has been developed. The proposed approach combines Hessian analysis and fuzzy connectedness segmentation. By detection shape information for different bone structure, the algorithm separates other bone structures from rib cage. The method is fully automatic with seed identification algorithm and the performance of the method has been evaluated on both small animal and human CT images from diverse subjects. The results found are promising with high accuracy and low time cost. As one limitation and future direction, current framework includes vertebral discs in the result and vertebrae bone structures are not individually numbered. To address this challenge, further tracking and identification will be needed with the help of shape and spatial information.

References

[1] Y. Kang, K. Engelke, and W.A. Kalender, "A new accurate and precise 3-D segmentation method for skeletal structures in volumetric CT data," *Medical Imaging, IEEE Transactions on*, vol. 22, no. 5, pp. 586–598, May 2003.

[2] A.P. Kiraly, S. Qing, and H. Shen, "A novel visualization method for the ribs within chest volume data," in *SPIE*, 2006, vol. 6141.

[3] J. Staal, B. van Ginneken, and M.A. Viergever, "Automatic rib segmentation and labeling in computed tomography scans using a general framework for detection, recognition and segmentation of objects in volumetric data," *Medical Image Analysis*, vol. 11, no. 1, pp. 35–46, 2007.

[4] J. Lee and A.P. Reeves, "Segmentation of individual ribs from low-dose chest CT," in *SPIE*, 2010, vol. 7624.

[5] L. Zhang, X. Li, and Q. Hu, "Automatic rib segmentation in chest CT volume data," in *iCBEB 2012*, May 2012, pp. 750–753.

[6] J.K. Udupa and S. Samarasekera, "Fuzzy connectedness and object definition: Theory, algorithms, and applications in image segmentation," *CVGIP: Graph. Model & Imag. Proc.*, vol. 58, no. 3, pp. 246–261, 1996.

[7] K.C. Ciesielski, J.K. Udupa, P.K. Saha, and Y. Zhuge, "Iterative relative fuzzy connectedness for multiple objects with multiple seeds," *Computer Vision and Image Understanding*, vol. 107, no. 3, pp. 160–182, 2007.

[8] A. Frangi, W. Niessen, K. Vincken, and M. Viergever, "Multiscale vessel enhancement filtering," in *MICCAI*, 1998, vol. 1496, pp. 130–137.

[9] Z. Xu, U. Bagci, A. Kubler, B. Luna, S. Jain, W. R. Bishai, and D.J. Mollura, "Computer-aided detection and quantification of cavitary tuberculosis from ct scans," *Medical Physics*, vol. 40, no. 11, 2013.

[10] U. Bagci, B. Foster, K. Miller-Jaster, B. Luna, B. Dey, W. Bishai, C. Jonsson, S. Jain, and D.J. Mollura, "A computational pipeline for quantification of pulmonary infections in small animal models using serial pet-ct imaging," *EJNMMI Research*, vol. 3, no. 1, pp. 55, 2013.